Measurement: Sensors xxx (xxxx) xxx

Contents lists available at ScienceDirect

Measurement: Sensors

journal homepage: www.sciencedirect.com/journal/measurement-sensors

Perspectives on multiparametric high-frequency impedance spectroscopy characterization of anatase TiO_2 nanotubes with nanoelectrode array sensors

ARTICLE INFO

Keywords:
Nano-electrode array
High frequency impedance spectroscopy
Titanium dioxide nanotubes
Multi-parametric characterization

ABSTRACT

Titanium dioxide nanotubes (TiO_2 NTs) are highly versatile materials for energy, sensing, environmental, and biomedical applications. This paper explores TiO_2 nanotube characterization and electrical imaging by high-frequency impedance spectroscopy (HFIS) with nanoelectrode array sensors. HFIS offers promising alternatives to traditional methods to characterize nanoscale objects, as it detects distinctive electrical and morphological features.

This work integrates: i) measurements with an advanced HFIS nanoelectrode array platform; ii) physics-based numerical simulations of the HFIS signal transduction mechanisms; iii) compact models for the estimation of geometrical and morphological parameters, to provide outlooks for the multiparametric characterization of single TiO_2 nanotubes at the platform sensitivity and resolution limits.

1. Introduction

Titanium dioxide nanotubes (TiO_2 NTs) have attracted considerable attention for several applications in the energy, sensing, environmental, and biomedical domains [1–5]. For instance, remarkable transduction capabilities of TiO_2 NTs for gas sensing have been extensively demonstrated [5,6]. In particular, the large surface area generated by the tubular morphology enhances the electrodes' sensitivity to gases, and the modification of the NT band structure through the incorporation of dopants improves the catalytic properties [5]. TiO_2 NTs also demonstrated technologically relevant properties for energy storage, including micro-batteries, supercapacitors, fuel cells [4], and dye-sensitized solar cells [7]. Last but not least, their utility extends to the biomedical domain, where they have been used as coatings for biomedical implants. In this context, TiO_2 NT layers have shown good adhesion, proliferation properties, and biocompatibility, making them suitable for applications in dental and cardiovascular stent applications [3,8]. Moreover, in powder form, TiO_2 NTs have shown efficacy for microbial disinfection and the degradation of pollutants [9]. The lack of fast, accurate, and low-cost, physical/morphological characterizations of single TiO_2 NTs is a notable limitation to their widespread use [10].

Indeed, achieving a good control of the TiO_2 electrical properties is fundamental for applications such as sensing and energy. Electrical and geometrical properties are usually characterized separately, and with traditionally bulky and expensive imaging technologies [11]. Robust and accurate multiparametric technologies simultaneously providing morphological and physical features would be extremely useful.

High-frequency impedance spectroscopy (HFIS) with nanoelectrode arrays [12] is an interesting option for multiparametric characterization of single TiO_2 nanotubes. HFIS with nanoelectrodes array enables spatially distributed detection, capacitance measurement, and imaging. Moreover, it has already proven its ability to detect distinctive impedance fingerprints, such as the conductive vs dielectric nature and the permittivity of single spherical analytes, and their dimensions down to decananometer scales [13–18].

The spectrally resolved high-frequency regime mitigates the AC potential decay in electrolytes (Debye screening). Indeed, in the field of impedance measuring systems with electrode arrays, where numerous recent studies have made significant contributions [19–29], the platform of this work remains one of the best in terms of array density, electrode size, spatial and capacitance resolution, and maximum measurement frequency [12,30].

The challenge is to characterize large aspect ratio TiO_2 NTs with dimensions and electrical response comparable to the spatial and capacitance detection limits of the technology.

Our study provides preliminary analysis and perspectives for TiO_2 nanotubes morphological and geometrical characterization integrating and matching physics-based numerical simulations and experimental results. Compact formulas are provided to estimate the NT projected length and in-plane rotation on the array. Physics-based numerical simulations with electrical parameters from the scientific literature and geometrical parameters extracted from SEM images are carried out and matched to the experimental results.

In the following, Section 2 describes the NT fabrication process, and the experimental and numerical simulations setups. The methods for the geometrical characterization are reported in Section 2.4. Results are reported and discussed in Section 3. Conclusions are drawn in Section 4.

2. Materials and methods

2.1. TiO_2 nanotube fabrication

The NTs were fabricated by the electrochemical anodization method [4]. First, 10 × 10 mm titanium foils were cleaned in an ultrasonic bath

https://doi.org/10.1016/j.measen.2024.101414

with acetone and ethanol. Anodization was carried out in a conventional two-electrode cell at room temperature, where titanium served as the working electrode and platinum as the counter electrode. The electrolyte was glycerol containing 0.5 wt% NH_4F and 2M H_2O. Anodization voltage and time were 20 V and 30 min, respectively. As-prepared samples were annealed at 400 °C for 3 hours. Morphological analysis of prepared material was carried out using field emission scanning electron microscopy (Carl-Zeiss, AURIGA Compact FIB-SEM). Structural characterization of materials was performed by Raman spectroscopy (Jasco NRS5100 confocal Raman microscope equipped with an excitation laser diode, laser wavelength 785 nm).

2.2. Experiments

The HFIS nanoelectrode (NE) array platform, based on a chip by NXP Semiconductors [12], is used to analyze nominally monodisperse solutions of the anatase TiO_2 NTs. The key features of the platform are summarized in the following.

Fig. 1a shows the experimental setup and the NE array chip. The latter features 256 × 256 individually addressable NEs, with a radius of 90 nm and pitch $p_x \times p_y = 600 \times 890$ nm. Once calibrated with the procedure described in Ref. [12], the platform measures the capacitance variation at each electrode ($\Delta C(i,j)$) induced by the NTs:

$$\Delta C = C_{w-analyte} - C_{w/o-analyte} \quad (1)$$

where $C_{w-analyte}$ and $C_{w/o-analyte}$ are the measured capacitance values with and without the analyte, respectively. Both are time average values over ≈100 consecutive measurements before and after the arrival of the NT, respectively. The platform has two main operation modes:

i) single frequency, when the capacitance is measured overtime for each of the 256 × 256 electrodes at one operating frequency (typically 50 MHz), resulting in a sampling rate of the entire array of ≈5.6 Hz.
ii) multi-frequency, when each NE capacitance is measured with N_F sequential frequency values within one frame. In this case, the frame rate is ≈ 0.075 Hz, depending on N_F and the frequency range considered.

The system implements temperature control (Peltier cell model ET-127-10-13-RS by Adaptive, PID temperature controller PR-59 by Laird Technologies) and the custom microfluidics described in Ref. [32], which is used to carry the sample in the measurement chamber. Fig. 1b sketches an NT over a portion of the NE array and defines the main geometrical and physical parameters of the system.

The θ and ϕ are the rotation angles in the vertical (x-z) and horizontal (x-y) plane and they span the [0, 90]° and [90, 90]° ranges, respectively. The NTs were detached from the Ti foil substrate and dispersed in 2 mL of deionized water and 2 mL of NaCl 150 mM solution, sonicated, and then introduced into the microfluidics chamber for the measurements. We employed an ultrasonic homogenizer CPX-750 by Cole Parmer with an operating frequency of 20 kHz at ≈ 500 W for 2 minutes. Analytes were detected as capacitance steps at each electrode by applying a moving-average algorithm to the time series of each electrode as in Refs. [13,17,32]. 85-th percentile outliers were removed based on the experimental cumulative distribution function of the 14 outermost electrodes (first and last rows) noise (experimental standard deviation) of the 7 × 7 sub-array around the detected object [17]. Additionally, the average ΔC of the 14 outermost electrodes in the 7 × 7 sub-array has been subtracted from the experimental data to eliminate unwanted drifts and offsets [17]. Finally, we verified the presence of single nanotubes in the analyzed solution. The 10 μL of the analyzed samples were dried on a SiO_2 substrate and cleaned with IPA to remove saline residues, this procedure was repeated 3 times to increase the nanotubes concentration on the substrate. For this analysis we employed the scanning electron microscope of a dual beam FIB-SEM FEI Strata DB235M, results are reported in Section 3.1.

2.3. Simulations

Numerical simulations of the sensor response were run with ENBIOS, an in-house, accurate CVFEM simulator that self-consistently solves the Poisson-Boltzmann equation and the coupled Poisson-Drift-Diffusion equations for all ion species in the electrolyte across the 3D domain of the NE array chip [33]. The effectiveness of the simulator in reproducing, predicting, and supporting the interpretation of experimental results has been widely explored and demonstrated [12,13,15,16,32,34]. The simulated 3D domain reproduces a portion of the experimental one (typically a 9 × 11 array, to reduce the impact of boundary conditions). The capacitance variation in the switching regime (according to the hardware measurement principle [12]) is derived from the AC numerical simulations as described in Ref. [12]. The values of the main geometrical and physical parameters (see Fig. 1b) are those in Table 1, if not otherwise stated. An important sanity check for the validation of the numerical simulation setup is that the capacitive response of the sensor to small (spherical) particles is expected to depend linearly on the analyte's volume (Ω) [37]. Fig. 2 shows numerical simulations of NTs with different wall-thickness T_{NT} and constant outer radius R_{NT}, thus

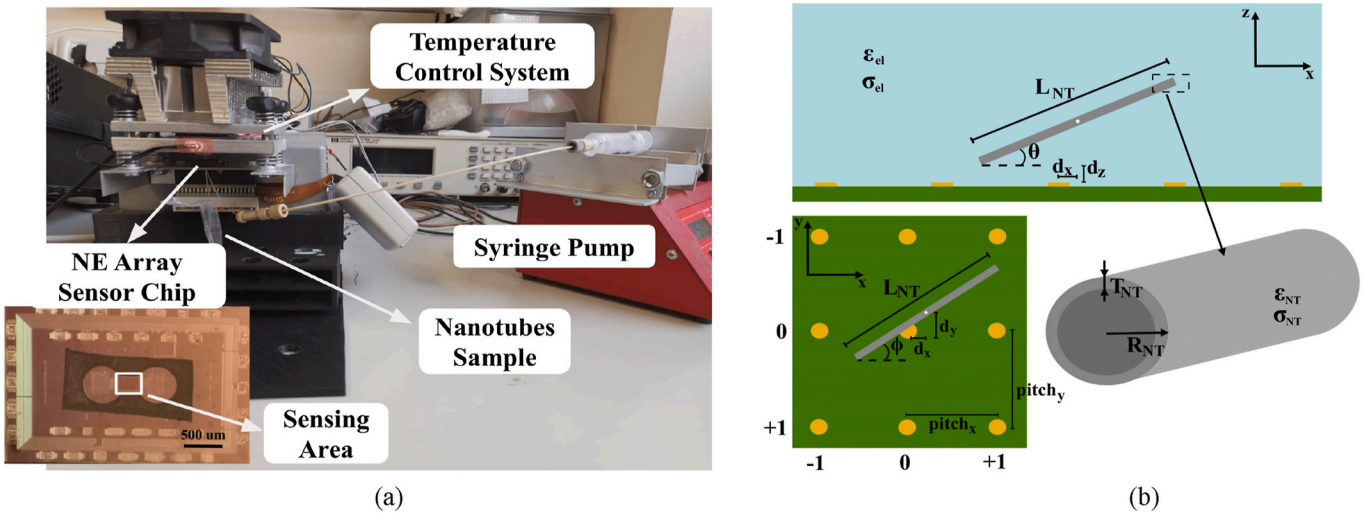

Fig. 1. (a) HFIS nanoelectrode array sensor platform. (b) Sketch of a nanotube over a 3 × 3 sub-array. The main geometrical and physical parameters are reported.

Table 1
HFIS parameters used in experiments and simulations.

Electrolyte	NaCl 150 mM, H_2O
Electrolyte relative permittivity ($\varepsilon_{r,el}$)	80
Single Frequency	50 MHz
Multi-Frequency	2–70 MHz, $N_F = 10$
NT relative permittivity ($\varepsilon_{r,NT}$)	48 (anatase TiO_2) [35]
NT conductivity (σ_{NT})	2 S/m [36]
NT length (L_{NT})	1200 nm (Fig. 3)
NT radius (R_{NT})	25 nm (Fig. 3)
NT wall thickness (T_{NT})	7 nm (Fig. 3)

Table 2
Ensemble average of the estimated parameters in NaCl and H_2O. Complete histograms are reported in Fig. 9.

	$\overline{L_{p,est}}$ (nm)	$\overline{\phi_{est}}$ (°)	$\overline{\theta_{est}}$ (°)
NaCl	900	14	41
H_2O	958	30	37

resulting in different NT volumes at constant NT centroid and d_z. The responses nicely follow straight lines that project to an extremely small $\Delta C \sim 1$ aF (smaller than the platform noise limit) for $\Omega_{NT} = 0$, as expected. These results confirm the validity of the simulation setup and support the use of the compact model of [37] also with non-spherical, high aspect ratio analytes such as the NTs of this work.

Numerical simulations were also used to gain insights into whether the detected objects are single NTs or a cluster of NTs (Cluster-NT). Due to limited computational resources, we focused on those clusters that are more difficult to discriminate from single nanotubes. Consistently, we calculated the sensor response approximating the cluster with a cylinder of the same length L as a single NT. The cylinder radius is computed as $R_{cluster} = \sqrt{V_{cluster}/\pi L}$ where $V_{cluster} = N \cdot \Omega_{NT}$, N is the number of NTs in the cluster and Ω_{NT} is the single NT volume. According to this choice, the cylinder has the same volume as the cluster; hence, at first order, the same response [37].

2.4. Approaches for multi-parametric characterization

Due to the higher sampling rate (see Section 2.2) single frequency electrical images are more suitable than multifrequency ones for extraction of key geometrical parameters, such as the NT projected length on the array. To this end, 3 × 3 sub-array electrical images (at 50 MHz) of individual NT (i and $j \in \{-1,0,1\}$) are analyzed. The choice for the sub-array size is justified according to results reported in Section 3.2.

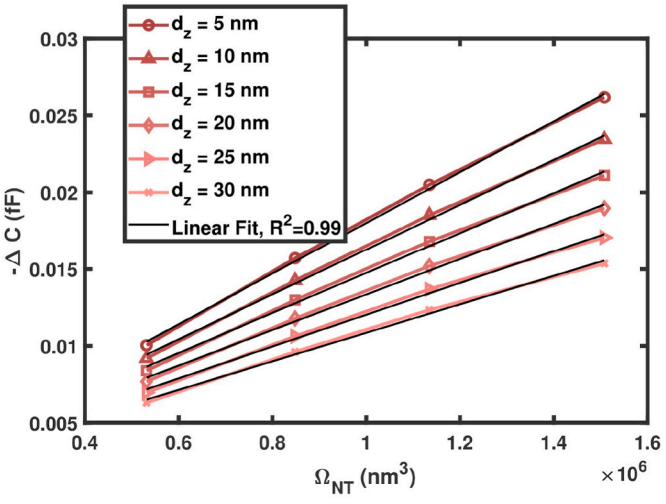

Fig. 2. Simulated nanoelectrode response (-ΔC) at 50 MHz in NaCl 150 mM as a function of the analyte volume Ω_{NT} for different vertical displacements (d_z). The volumes correspond to $T_{NT} = 3$, 5, 7, and 10 nm and constant $R_{NT} = 25$ nm. (d_x, d_y)=(0,0) nm. Other parameters are reported in Table 1.

The central electrode (0, 0) of the chosen sub-array is by definition the one with the largest (in absolute value) ΔC response. The center of the central electrode is by definition the origin of the cartesian reference system. The NT projected length ($L_{p,est}$) on the array plane is estimated by averaging the pixel distances by the corresponding measured Δ$C(i,j)$:

$$L_{p,est} = \sqrt{\frac{\sum_{ij} \Delta C\,(i,j) \cdot d(i,j)^2}{\sum_{ij} \Delta C(i,j)}} \tag{2}$$

$$\text{with}: d(i,j)^2 = (i \cdot p_x)^2 + \left(j \cdot p_y\right)^2$$

where $p_x = 600$ nm, and $p_y = 890$ nm for this work. According to (2) the estimation is in principle independent of ϕ, because the equations leverage on the known electrodes' position in the 2D plane. This condition has been verified by applying (2) to numerical simulations with varying ϕ (±30°, ±60°, 90°). The variation in $L_{p,est}$ is limited to lower than 2 %.

The rotation angle in the horizontal plane ϕ can be estimated (with bias) by exploiting the array's central symmetry and by knowing the array geometry. In particular, for each electrode (i,j) ≠ (0,0), the angle between the axis passing through the center of electrode (i,j) and the center of electrode (0,0) and the positive horizontal axis ($\phi_{i,j}$) is weighted by the ΔC at electrode (i,j), thus finding ϕ_{est} as:

$$\phi_{est} = \frac{\sum_{ij} \Delta C(i,j) \cdot \phi_{i,j}}{\sum_{ij} \Delta C(i,j)} \tag{3}$$

$$\text{with}: \phi_{i,j} = \begin{cases} \phi(i,j) = \tan^{-1}\left(\dfrac{j \cdot p_y}{i \cdot p_x}\right) \\ \phi(-i,-j) = \phi(i,j) \end{cases}$$

The central electrode (i,j) = (0,0) is excluded from the summation since it is assumed that rotations of the NT around the electrode of maximum response (hence, minimum distance from the NT) do not affect the ΔC(0,0).

For a 3 × 3 array and (p_x, p_y) = (600, 890) nm:

$$\phi_{i,j} = \begin{pmatrix} -56^\circ & 90^\circ & 56^\circ \\ 0^\circ & excl. & 0^\circ \\ 56^\circ & 90^\circ & -56^\circ \end{pmatrix} \tag{4}$$

As regards the electrical properties of a single NT (highly relevant for energy and sensing applications), HFIS has already been shown by experiments and simulations to discriminate relative dielectric permittivity of the analyte [15,18]. In this work, the physical and geometrical properties in Table 1 are confirmed by direct comparison between measured and simulated capacitance spectra for single-NTs in NaCl solution, see Section 3.4.

3. Results and discussion

3.1. TiO_2 nanotubes fabrication results

Morphological observations (Fig. 3a and b) indicate the synthesis of well-oriented NTs with an average diameter of approximately 50 nm and wall thickness of 7 nm. The average length of the tubes is 1200 nm. Fig. 4 illustrates the Raman spectrum of the NTs. It shows Raman active modes at 144 cm^{-1}, 399 cm^{-1}, 516 cm^{-1}, and 639 cm^{-1}, which can be ascribed to the anatase crystalline phase of TiO_2 [31].

Fig. 5 shows a representative image of a single nanotube observed in

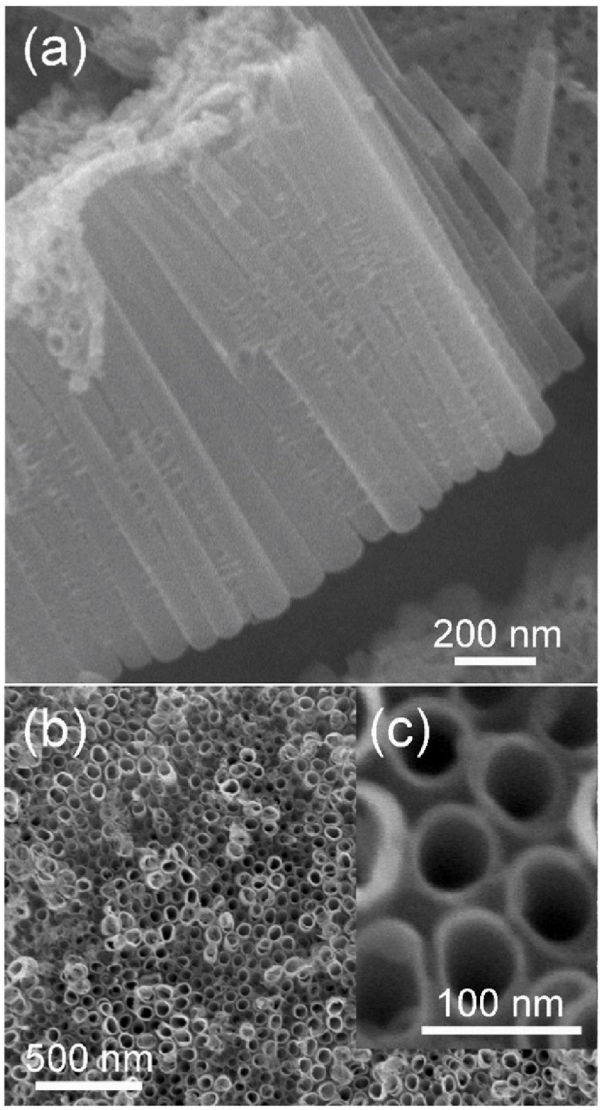

Fig. 3. SEM images of the fabricated TiO_2 NTs: (a) lateral image of TiO_2 NTs; (b) and (c) surface images of TiO2 NTs at different magnifications.

the analyzed solution.

3.2. Estimated detection limits for TiO_2 nanotubes

In this section, we explore by simulation the implications of the nanoelectrode array platform noise floor (about 1–2 aF) on the accuracy of the NT detection and physical/geometrical parameter extraction procedures outlined in Sect. 2. The main novelty we encounter is the combination of extremely small diameter and wall thickness with the large aspect ratio of the NTs. The expected large value of the relative dielectric permittivity also reduces the image contrast with respect to the electrolyte. As a result, the order of magnitude of the ΔC is only a few tens of aF, which is close to the noise limit of the system [12,13].

The simulated ΔC for anatase TiO_2 NTs with the material parameters of Table 1 and different wall thickness, T_{NT}, elevation, d_z, electrolytes, and measurement frequencies, is always negative, as expected for uncharged dielectric materials [12,13,15,32], see for instance Figs. 2, 6a and 6b.

In order to identify the optimum size of a single NT image for parametric characterization, we start observing that the nominal length of the NTs (1200 nm) exactly matches the $2{\cdot}p_x$ value, and it is lower than $2{\cdot}p_y$. If we set the electrode with maximum response in the center of the

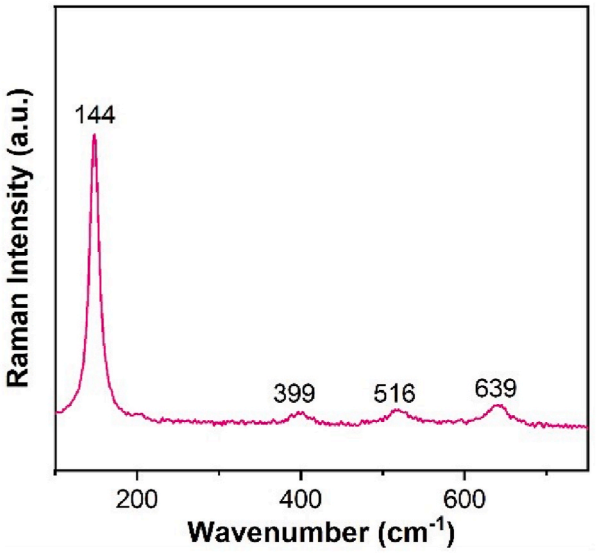

Fig. 4. Raman spectrum of fabricated TiO_2 NTs, which shows peaks that correspond to the anatase crystalline phase of TiO_2.

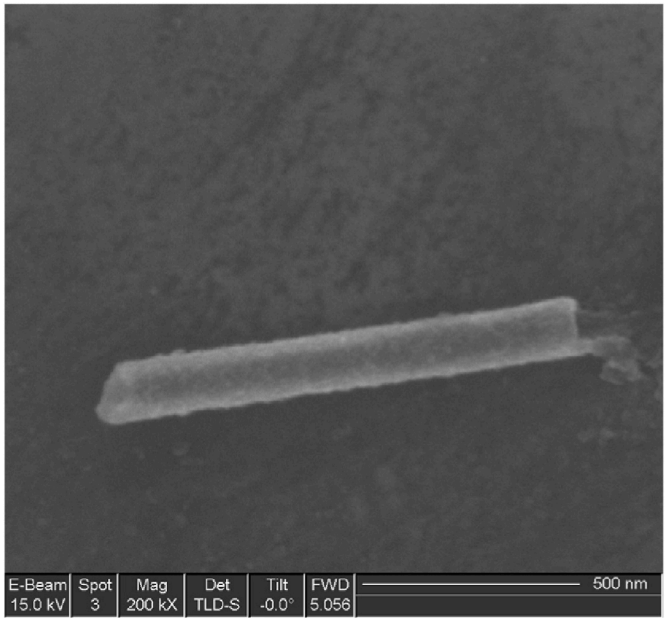

Fig. 5. SEM image of a single-nanotube identified in the analyzed solution.

NT capacitance image, then a 3 × 3 sub-array is always sufficient to enclose the NT. Larger sub-arrays would only introduce unwanted noise in the NT image; hence, in the parameters extracted with Eqs. (2) and (3), as discussed below.

Fig. 6a confirms the validity of this choice by showing the mean and the minimum (highest response, since $\Delta C < 0$) response of the electrodes at the edge of a 5 × 5 array having an NT inclined at different ϕ angles for deionized H_2O and 150 mM NaCl solution. The $|\Delta C|$ is ≤ 0.15 aF, i.e. one order of magnitude lower than the typical measurement noise [12, 13].

Additional simulations with varying θ bring to the same conclusion. Indeed, Fig. 6b shows the simulated ΔC for the worst case scenario of a single NT at $\phi = 0°$, $L_{NT} = 2{\cdot}p_x$, $(d_x, d_y, d_z) = (0, 0, 20)$ nm, and $\theta \in [0, 25]°$. For $\theta \geq 5°$ the central electrode of the original sub-array is no more the one with the largest $|\Delta C|$, as evident from the green line (electrode (0,0)) approaching zero faster than the red line (electrode (0, −1)).

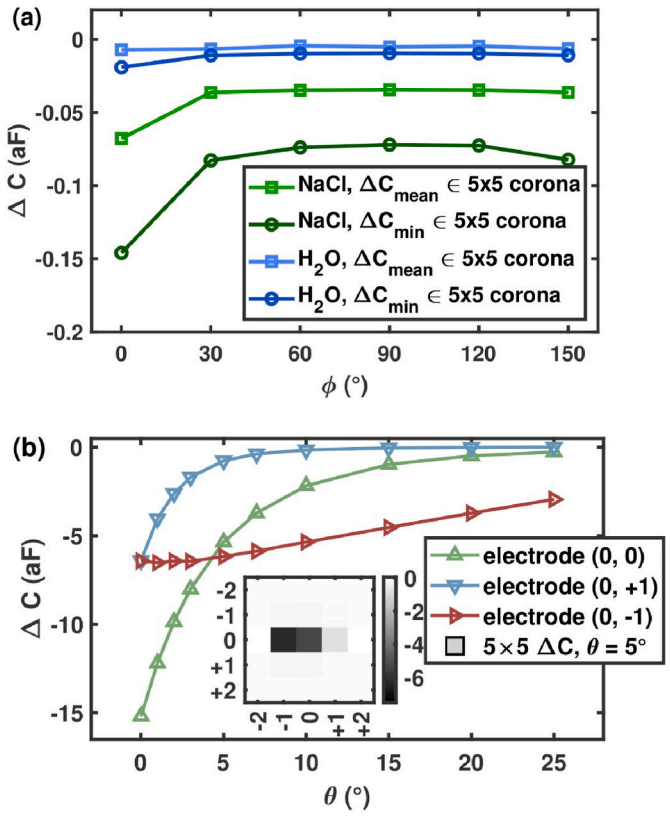

Fig. 6. Simulated ΔC for a single NT at 50 MHz, $(d_x, d_y, d_z) = (0, 0, 20)$ nm and parameters as in Table 1. (a) Mean and minimum of values of the electrodes surrounding the 3 × 3 central sub-array for deionized water and 150 mM NaCl solution. (b) ΔC as a function of θ at electrode (0, −1), (0, 0), and (0, +1). The inset shows a typical 5 × 5 sub-array response at $\theta = 5°$ (with 150 mM NaCl electrolyte).

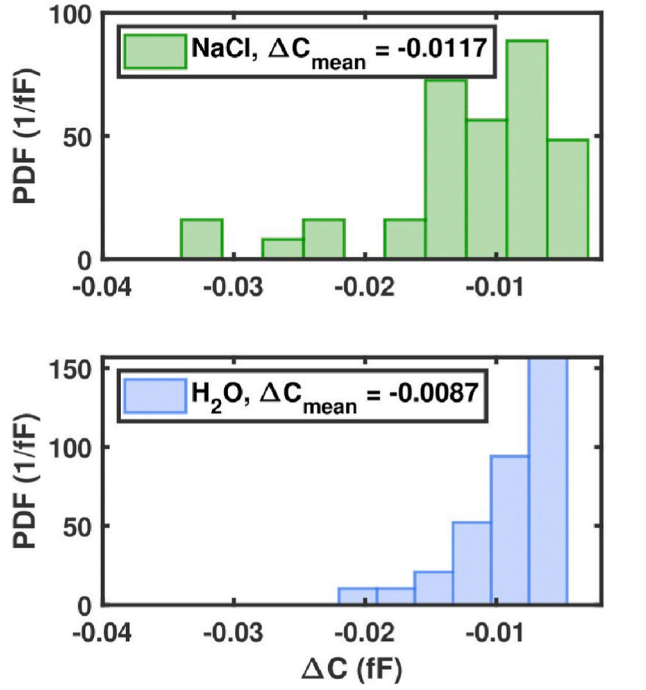

Fig. 7. PDFs of the experimental ΔC in NaCl and H_2O solution in single frequency (50 MHz) operation mode, after data elaboration and outliers exclusion described in Section 2.2.

Therefore the 3 × 3 sub-array shifts one position to the left. When this happens, however, the $|\Delta C|$ for the electrode (0, +1) is already <0.7 aF, essentially undetectable in real measurements. Simulations with $\phi = 45°$ and 90° (not shown), lead to the same conclusion.

Therefore, consistently with previous investigations on spherical nanoparticles of comparable size [13,32], we conclude that a 3 × 3 sub-array centered on the electrode (pixel) with maximum response is sufficient to investigate individual NTs of the explored length, regardless of their in-plane and out-of-plane orientation.

Fig. 10 shows the simulated capacitance response as a function of the Cluster-NT size. As expected the $|\Delta C|$ is higher as the NT cluster size increases. The mean measured value is compatible with the numerical simulation of single NT or tiny clusters, the outliers are indeed more likely to be cluster-NT up to 5 × 5 size.

3.3. Extraction of geometrical features

The object detection and data elaboration procedures described in Section 2 led to identify 15 samples in H_2O and 15 samples in NaCl solutions, respectively, having a $|\Delta C(0,0)|$ larger than 2 × the experimental standard deviation of the capacitance signals and a pixelated ΔC response attributable to a cylindrical-shape analyte. Fig. 7 shows the distributions of the measured ΔC values. We see that, on average, the ΔCs are larger (in absolute value) for NaCl solution than for deionized water, as expected.

Fig. 8 shows typical 3 × 3 ΔC maps of two NTs (sketched in red according to the estimated $L_{p,est}$ and ϕ_{est}) over the nanoelectrode array for NaCl and H_2O solutions.

Fig. 9 reports the estimated projected length $L_{p,est}$ and in-plane rotation angle ϕ_{est} using Eqs. (2) and (3) on experimental data, respectively. The mean value of ϕ_{est} is close to the expected one ($\simeq 20°$, i.e. mean value of the $\phi_{i,j}$ matrix in (4)). As for the $L_{p,est}$, similar values are found for both electrolyte solutions, which are smaller than the nominal L_{NT} measured from Fig. 3. This result can be due to: a non-zero tilt of the NTs in the vertical direction ($\theta \neq 0$ on average), a rupture of the NTs (upon detachment from the substrate or during the solution sonication phases), or both.

Considering the former hypothesis ($\theta \neq 0$), from a simple geometrical analysis of Fig. 1b we can estimate the elevation angle θ_{est} according to:

$$\cos(\theta_{est}) = \frac{L_{p,est}}{L_{NT}} \tag{5}$$

Equation (5) then yields $\theta \simeq 37°$ and 41° for H_2O and NaCl solutions respectively, as reported in Table 2.

Note that an inherent ambiguity exists for elongated nanoscale objects with a size comparable to the array's pitch, between the centroid position (d_x, d_y) and the vertical orientation angle, θ. Indeed, two such objects, one with elevation angle $\theta \neq 0$ and $(d_x, d_y) = (0, 0)$ nm, and the other with $\theta = 0$ and $(d_x, d_y) \neq (0,0)$ nm, can produce very similar single frequency capacitance images. In fact, the ΔC depends on both the volume of the NT's portion in proximity of the examined electrode and the unperturbed electric field at the analyte's position [37]. The elevation of one of the object's extremes and the horizontal displacement of the object independently affect both these quantities, resulting in highly similar pixelated capacitance responses. The analysis of large sets of capacitive spectra with advanced statistical methods such as, for instance, Bayesian inversion and machine learning, could possibly address this issue.

3.4. Comparison between measured and simulated spectra

Figs. 11 and 12 show the nanotubes' experimental spectra in NaCl solution. Numerical simulations with parameters reported in Table 1 are also reported. In particular, Fig. 11 shows the simulated spectrum of a single-NT, which agrees well with the average measured spectra. Since

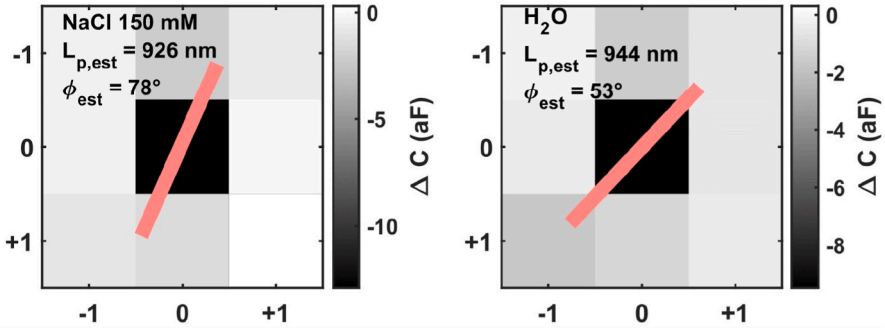

Fig. 8. Typical 3 × 3 results of an NT measured with nanoelectrode array in single frequency (50 MHz) mode in NaCl and H_2O. The central electrode (0,0) is the one with the highest response by definition. The NT with estimated approximate L_p and ϕ is depicted.

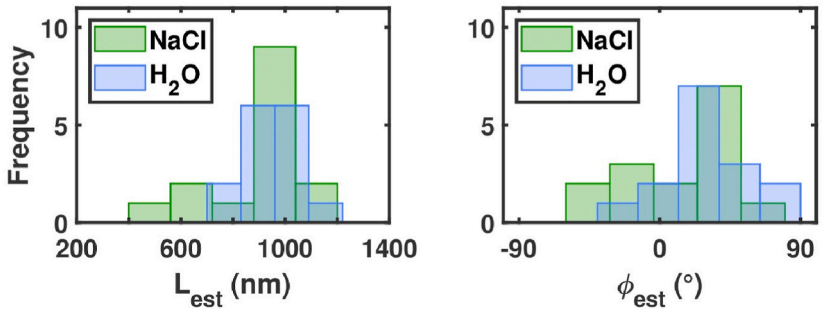

Fig. 9. Histograms of $L_{p,est}$ and ϕ_{est} from experimental results and Eqs. (2) and (3) respectively, for NTs in NaCl solution and deionized water at 50 MHz. The mean values of these distributions are reported in Table 2.

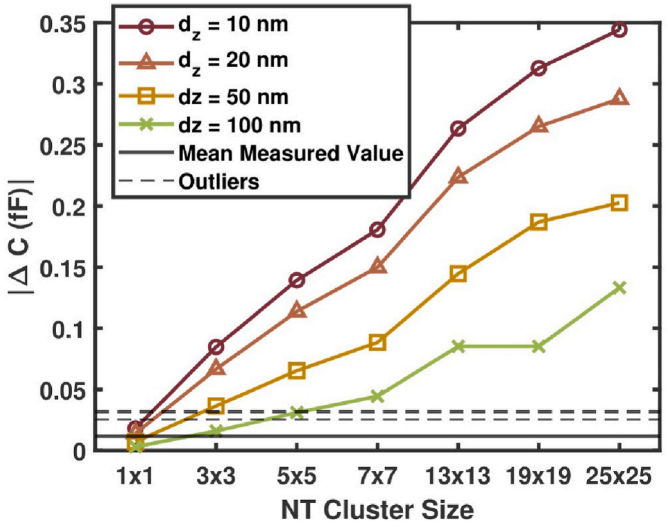

Fig. 10. Numerical simulation of the capacitance response $|\Delta C|$ as a function of the cluster size for different d_z values. The mean measured value and the 5th percentile outliers of distributions in Fig. 7 are also shown.

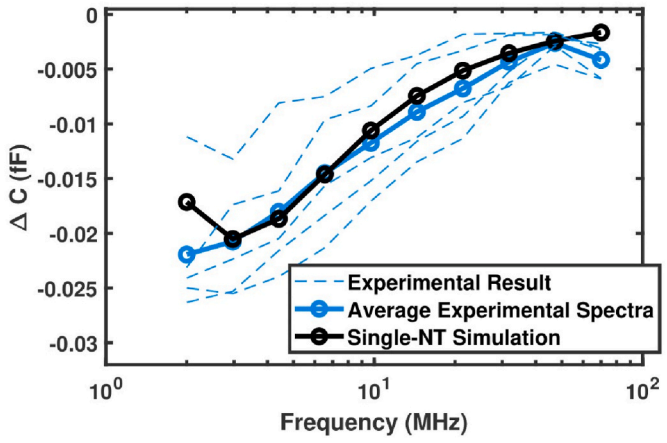

Fig. 11. Experimental results of expected single-NT and numerical simulation matching the average spectra. The simulated (ϕ, θ, d_z) are (0°, 0°, 100 nm) and parameters reported in Table 1.

the single-NT simulation was performed with $d_z = 100$ nm, a cluster-NT would match the experimental results only with a higher d_z which is unlikely to be the case based on past analysis of d_z distributions in the sensor [32]. On the other hand, the experimental spectrum in Fig. 12 are less likely to be those of a single-NT, since it agrees with a numerical simulation of a 3 × 3 cluster at $d_z = 75$ nm, which is comparable to the simulation reported in Fig. 11.

4. Conclusion

We report, for the first time to our knowledge, high frequency impedance spectroscopy of single TiO_2 nanotubes featuring a very high aspect ratio. Our work proposes a few simple equations for a first-order characterization of the basic geometrical parameters of these cylindrical analytes. The object detection and estimation procedure avails itself of accurate two-dimensional numerical simulations of the sensor response, which help identify the best conditions (especially image size) for the purpose.

Although this work still lacks a statistically large experimental dataset, and despite inherent parameter correlations (which give rise to non-unique parameter sets matching equally well some of the sensor

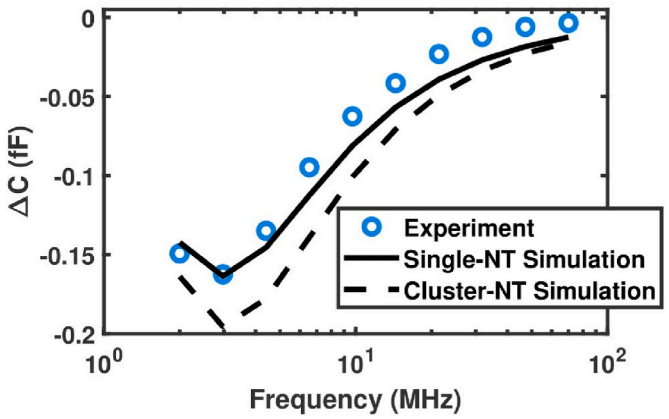

Fig. 12. Measured and simulated spectra of a single-NT and a 3 × 3 cluster in 150 mM, NaCl solution environment, for $d_x = d_y = 0$, $\theta = 0°$. For the single-NT $(\phi, \theta, d_z) = (0°, 0°, 6\text{ nm})$, $(\phi, \theta, d_z) = (0°, 0°, 75\text{ nm})$, all the other parameters are those reported in Table 1.

responses), this preliminary work suggests that useful indications on the nanotube length, orientation, and clustering can be extracted from capacitance images utilizing nanoelectrode arrays.

Simulations of the spectral response, consistent with the parameters estimated from single frequency data, yield good agreement with experiments, thus indirectly confirming the values of the dielectric properties of single NTs derived from the literature. More extensive measurements and simulations, possibly leveraging Bayesian inversion and machine learning statistical methods, will likely provide new insights on the charge state and the exact positioning of the NTs on the array, both being important for NTs characterization.

Acknowledgment

The authors would like to thank F. Widdershoven (NXP Semiconductors) for providing the chip and for fruitful discussions, C. Ongaro, L. Orazi, B. Zardin, and M. Borghi (UniMoRe) for the design of the PDMS ring and for fruitful discussions, C. Fontanesi (UniMoRe) for providing the sonicating equipment, C. Menozzi (UniMoRe) for the acquisition of single-nanotubes SEM images, and J. Nicolini (UniMoRe) for fruitful discussion. This work was supported in part by ESF REACT-EU for National Operational Programme (PON) Research and Innovation 2014–2020 and by the European Union, NextGenerationEU initiative via Linea di Investimento 1.3 Partenariati Estesi Area 6 the PNRR HEAL ITALIA Project PE 0000019. V. Galstyan and P. D'Angelo acknowledge the Project funded under the National Recovery and Resilience Plan (NRRP), Mission 04 Component 2 Investment 1.5 – NextGenerationEU, Call for tender n. 3277 dated December 30, 2021, Award Number: 0001052 dated June 23, 2022.

References

[1] B.L. Ellis, P. Knauth, T. Djenizian, Three-dimensional self-supported metal oxides for advanced energy storage, Adv. Mater. 26 (2014) 3368–3397, https://doi.org/10.1002/adma.201306126, 6.

[2] O. Zakir, A. Ait-Karra, R. Idouhli, M. Khadiri, B. Dikici, A. Aityoub, A. Abouelfida, A. Outzourhit, A review on TiO2 nanotubes: synthesis strategies, modifications, and applications, J. Solid State Electrochem. 27 (2023) 2289–2307, https://doi.org/10.1007/s10008-023-05538-2, 9.

[3] M.F. Kunrath, R. Hubler, R.S.A. Shinkai, E.R. Teixeira, Application of TiO2 nanotubes as a drug delivery system for biomedical implants: a critical overview, ChemistrySelect 3 (2018) 11180–11189, https://doi.org/10.1002/slct.201801459, 10.

[4] V. Galstyan, J.M. Macak, T. Djenizian, Anodic TiO2 nanotubes: a promising material for energy conversion and storage, Appl. Mater. Today 29 (2022) 101613, https://doi.org/10.1016/j.apmt.2022.101613, 12.

[5] V. Galstyan, E. Comini, G. Faglia, G. Sberveglieri, TiO2 nanotubes: recent advances in synthesis and gas sensing properties, Sensors 13 (2013) 14813–14838, https://doi.org/10.3390/s131114813, 10.

[6] X. Tian, X. Cui, T. Lai, J. Ren, Z. Yang, M. Xiao, B. Wang, X. Xiao, Y. Wang, Gas sensors based on TiO2 nanostructured materials for the detection of hazardous gases: a review, Nano Mater. Sci. 3 (2021) 390–403, https://doi.org/10.1016/j.nanoms.2021.05.011, 12.

[7] X. Hou, K. Aitola, P.D. Lund, TiO2 nanotubes for dyesensitized solar cells-A review, Energy Sci. Eng. 9 (2021) 921–937, https://doi.org/10.1002/ese3.831, 7.

[8] Y. Cheng, H. Yang, Y. Yang, J. Huang, K. Wu, Z. Chen, X. Wang, C. Lin, Y. Lai, Progress in TiO2 nanotube coatings for biomedical applications: a review, J. Mater. Chem. B 6 (2018) 1862–1886, https://doi.org/10.1039/C8TB00149A.

[9] W.A. Abbas, I.H. Abdullah, B.A. Ali, N. Ahmed, A.M. Mohamed, M.Y. Rezk, N. Ismail, M.A. Mohamed, N.K. Allam, Recent advances in the use of TiO2 nanotube powder in biological, environmental, and energy applications, Nanoscale Adv. 1 (2019) 2801–2816, https://doi.org/10.1039/C9NA00339H.

[10] R. Herrera-Basurto, Angela Inmaculada Lopez-Lorente, M. Valcarcel, Scanning electron microscopy of carbon nanotubes dispersed in ionic liquid: solvent influence study, Microchem. J. 122 (2015) 137–143, https://doi.org/10.1016/j.microc.2015.04.012, 9.

[11] T. Belin, F. Epron, Characterization methods of carbon nanotubes: a review, Mater. Sci. Eng., B 119 (2005) 105–118, https://doi.org/10.1016/j.mseb.2005.02.046, 5.

[12] F. Widdershoven, A. Cossettini, C. Laborde, A. Bandiziol, P.P.V. Swinderen, S. G. Lemay, L. Selmi, A CMOS pixelated nanocapacitor biosensor platform for high-frequency impedance spectroscopy and imaging, IEEE Trans. Biomed. Circu. Sys. 12 (2018), https://doi.org/10.1109/TBCAS.2018.2861558.

[13] D. Goldoni, L. Rovati, L. Selmi, Towards continuous nano-plastic monitoring in water by high frequency impedance measurement with nano-electrode arrays, IEEE Sensor. J. (2023) 1, https://doi.org/10.1109/JSEN.2023.3296158, 1.

[14] A. Cossettini, B. Stadlbauer, J.A. Morales, L. Taghizadeh, L. Selmi, C. Heitzinger, Determination of Micro- and Nanoparticle Properties by Multi-Frequency Bayesian Methods and Applications to Nanoelectrode Array Sensors, 2019-October, 2019, https://doi.org/10.1109/SENSORS43011.2019.8956529.

[15] A. Cossettini, C. Laborde, D. Brandalise, F. Widdershoven, S.G. Lemay, L. Selmi, Space and frequency dependence of nanocapacitor array sensors response to microparticles in electrolyte, IEEE Sensor. J. 21 (2021), https://doi.org/10.1109/JSEN.2020.3032712.

[16] C. Laborde, F. Pittino, H.A. Verhoeven, S.G. Lemay, L. Selmi, M.A. Jongsma, F. P. Widdershoven, Real-time imaging of microparticles and living cells with CMOS nanocapacitor arrays, Nat. Nanotechnol. 10 (2015), https://doi.org/10.1038/nnano.2015.163.

[17] F. Lombardo, F. Pittino, D. Goldoni, L. Selmi, Machine learning and data augmentation methods for multispectral capacitance images of nanoparticles with nanoelectrodes array biosensors, Eng. Appl. Artif. Intell. 127 (2024) 107246, https://doi.org/10.1016/j.engappai.2023.107246, 1.

[18] C. Renault, C. Laborde, A. Cossettini, L. Selmi, F. Widdershoven, S.G. Lemay, Electrochemical characterization of individual oil micro- droplets by high-frequency nanocapacitor array imaging, Faraday Discuss 233 (2021), https://doi.org/10.1039/D1FD00044F.

[19] J. Abbott, A. Mukherjee, W. Wu, T. Ye, H.S. Jung, K.M. Cheung, R.S. Gertner, M. Basan, D. Ham, H. Park, Multiparametric functional imaging of cell cultures and tissues with a CMOS microelectrode array, Lab Chip 22 (2022), https://doi.org/10.1039/D1LC00878A.

[20] K. Hu, C.E. Arcadia, J.K. Rosenstein, A large-scale multimodal CMOS biosensor array with 131,072 pixels and codedivision multiplexed readout, IEEE Solid-State Circu. Lett. 4 (2021), https://doi.org/10.1109/LSSC.2021.3056515.

[21] D. Jung, G.V. Junek, J.S. Park, S.R. Kumashi, A. Wang, S. Li, S.I. Grijalva, N. Fernandez, H.C. Cho, H. Wang, A CMOS 21 952-pixel multi-modal cell-based biosensor with four-point impedance sensing for holistic cellular characterization, IEEE J. Solid State Circ. 56 (2021), https://doi.org/10.1109/JSSC.2021.3085571.

[22] K. Hu, J. Ho, J.K. Rosenstein, Super-resolution electrochemical impedance imaging with a 512 x 256 CMOS sensor array, IEEE Trans. Biomed. Circu. Sys. 16 (2022) 502–510, https://doi.org/10.1109/tbcas.2022.3183856, 8.

[23] P.H. Lai, L.S. Tseng, C.M. Yang, M.S. Lu, Design and characterization of a 16 x 16 CMOS capacitive DNA sensor array, IEEE Sensor. J. (2023), https://doi.org/10.1109/JSEN.2023.3253123.

[24] S. Kumashi, D. Jung, J. Park, S. Tejedor-Sanz, S. Grijalva, A. Wang, S. Li, H.C. Cho, C. Ajo-Franklin, H. Wang, A CMOS multi-modal electrochemical and impedance cellular sensing array for massively paralleled exoelectrogen screening, IEEE Trans. Biomed. Circu. Sys. 15 (2021), https://doi.org/10.1109/TBCAS.2021.3068710.

[25] D. Lee, D. Jung, F. Jiang, G.V. Junek, J. Park, H. Liu, Y. Kong, A. Wang, Y. Kim, K.-S. Choi, J. Wang, H. Wang, A multifunctional CMOS biosensor array with on-chip dep-assisted sensing for rapid low-concentration analyte detection and close loop particle manipulation with no external electrodes, IEEE Trans. Biomed. Circu. Sys. 17 (2023) 1214–1226, https://doi.org/10.1109/TBCAS.2023.3343068, 12.

[26] S. Chitale, W. Wu, A. Mukherjee, H. Lannon, P. Suresh, I. Nag, C.M. Ambrosi, R. S. Gertner, H. Melo, B. Powers, H. Wilkins, H. Hinton, M. Cheah, Z.G. Boynton, A. Alexeyev, D. Sword, M. Basan, H. Park, D. Ham, J. Abbott, A semiconductor 96-microplate platform for electrical-imaging based high-throughput phenotypic screening, Nat. Commun. 14 (2023) 7576, https://doi.org/10.1038/s41467-02343333-9, 11.

[27] L.H. Lai, W.Y. Lin, Y.W. Lu, H.Y. Lui, S. Yoshida, S.H. Chiou, C.Y. Lee, A 460 800 pixels cmos capacitive sensor array with programmable fusion pixels and noise canceling for life science applications, IEEE Trans. Circu. Sys. II: Express Briefs 70 (2023) 1734–1738, https://doi.org/10.1109/TCSII.2023.3261445, 5.

[28] P.S. Joshi, K. Hu, J.W. Larkin, J.K. Rosenstein, Programmable electrochemical stimulation on a large-scale CMOS microelectrode array, in: IEEE Biomedical Circuits and Systems Conference (BioCAS) 10, 2022, pp. 439–443, https://doi.org/10.1109/BioCAS54905.2022.9948674.

[29] H.O. Tabrizi, S. Forouhi, E. Ghafar-Zadeh, A high dynamic range dual 8x16 capacitive sensor array for life science applications, IEEE Trans. Biomed. Circu. Sys. 16 (2022) 1191–1203, https://doi.org/10.1109/TBCAS.2022.3230668, 12.
[30] A. Cossettini, D. Brandalise, P. Palestri, A. Bertacchini, M. Ramponi, F. Widdershoven, L. Benini, L. Selmi, Ultra-high frequency (500 MHz) capacitance spectroscopy for nanobiosensing, IEEE Sensors (2020), https://doi.org/10.1109/SENSORS47125.2020.9278583.
[31] E. Barborini, I.N. Kholmanov, P. Piseri, C. Ducati, C.E. Bottani, P. Milani, Engineering the nanocrystalline structure of tio2 films by aerodynamically filtered cluster deposition, Appl. Phys. Lett. 81 (2002) 3052–3054, https://doi.org/10.1063/1.1510579, 10.
[32] D. Goldoni, C. Ongaro, L. Orazi, L. Rovati, L. Selmi, Estimation of analyte's vertical positions above the surface of nanocapacitor array biosensors, IEEE Sensors (2023) 14, https://doi.org/10.1109/SENSORS56945.2023.10325169.
[33] F. Pittino, L. Selmi, Use and comparative assessment of the CVFEM method for Poisson-Boltzmann and Poisson-nernstplanck three dimensional simulations of impedimetric nanobiosensors operated in the DC and AC small signal regimes, Comput. Methods Appl. Mech. Eng. 278 (2014), https://doi.org/10.1016/j.cma.2014.06.006.
[34] A. Cossettini, L. Selmi, On the response of nanoelectrode impedance spectroscopy measures to plant, animal, and human viruses, IEEE Trans. NanoBioscience 17 (2018), https://doi.org/10.1109/TNB.2018.2826919.
[35] I. Ali, M. Suhail, Z.A. Alothman, A. Alwarthan, Recent advances in syntheses, properties and applications of TiO2 nanostructures, RSC Adv. 8 (2018) 30125–30147, https://doi.org/10.1039/C8RA06517A.
[36] S.K. Kajli, D. Ray, S.C. Roy, Morphology dependent electrical conduction and breakdown in single TiO2 nanotubes, Nanoscale Adv. 3 (2021) 432–445, https://doi.org/10.1039/D0NA00713G.
[37] F. Pittino, P. Scarbolo, F. Widdershoven, L. Selmi, Derivation and numerical verification of a compact analytical model for the ac admittance response of nanoelectrodes, suitable for the analysis and optimization of impedance biosensors, IEEE Trans. Nanotechnol. 14 (2015), https://doi.org/10.1109/TNANO.2015.2434106.

Daniele Goldoni[a,*], Vardan Galstyan[a,b], Luca Nappi[c], Francesco Rossella[c], Pasquale D'Angelo[b], Luigi Rovati[a], Luca Selmi[a]

[a] *Deptartment of Engineering "Enzo Ferrari" (DIEF), University of Modena and Reggio Emilia, Modena, Italy*

[b] *Institute of Materials for Electronics and Magnetism, National Research Council (IMEM-CNR), Parma, Italy*

[c] *Department of Physics, Informatics and Mathematics, University of Modena and Reggio Emilia, Modena, Italy*

[*] Corresponding author.
E-mail address: daniele.goldoni@unimore.it (D. Goldoni).